Applied Catalysis B: Environmental 252 (2019) 174–186

Contents lists available at ScienceDirect

Applied Catalysis B: Environmental

journal homepage: www.elsevier.com/locate/apcatb

# Facile fabrication of Ag/graphene oxide/$TiO_2$ nanorod array as a powerful substrate for photocatalytic degradation and surface-enhanced Raman scattering detection

Yanfen Wang[a,b], Miao Zhang[a], Hai Yu[a], Yong Zuo[a], Juan Gao[b], Gang He[a], Zhaoqi Sun[a,*]

[a] School of Physics & Materials Science, Anhui University, Hefei, 230601, PR China
[b] School of Materials Science and Engineering, Anhui University of Science and Technology, Huainan, 232001, PR China

ARTICLE INFO

*Keywords:*
SERS
$TiO_2$
Synergistic effect
Ag
Photocatalytic

ABSTRACT

A novel graphene oxide/$TiO_2$ nanorod array (GO/TNR) decorated with Ag nanoparticles (NPs) is successfully prepared as a photocatalyst and a surface-enhanced Raman scattering (SERS) substrate for organic molecule detection. The as-obtained Ag/GO/TNR sample exhibited a large specific surface area and high adsorption capacity toward Rhodamine 6G (R6G) molecules. Moreover, the GO interlayer with suitable content had a significant effect on the absorption intensity of light and Raman signals for the Ag/GO/TNR substrate. For R6G as probe molecules, the Ag/GO/TNR substrate with 5 min of GO-deposition achieved a lower detection limit of $1.0 \times 10^{-12}$ M and an improved enhancement factor (EF) of $5.86 \times 10^5$ as compared to other films. Furthermore, the relative standard deviation (RSD) value of the Raman vibration at 1650 $cm^{-1}$ cm was approximately 8.71%, and the good uniformity remained. Using Xenon lamp irradiation, the outstanding photocatalytic ability endowed the substrate with good self-cleaning and reusable properties. Based on the above results, a synergistic effect of three components (Ag NPs, GO interlayer, and TNR) is proposed to produce an excellent SERS performance, namely, a large adhesion area, the interaction of excited photons, and high-density hotspots in the active substrate.

## 1. Introduction

Surface-enhanced Raman scattering (SERS) is a fast and powerful analytic technique that has attracted great interest in chemistry and environmental monitor due to its high sensitivity, good surface selectivity, and unique chemical specificity (vibrational Raman scattering) [1–3]. Generally speaking, there are two types of enhancement mechanisms for high Raman signals: an electromagnetic mechanism (EM) and a chemical mechanism (CM). The former primarily originates from the enhanced local electromagnetic field caused by the plasmon resonance that emanates from the metal surface, which can generate many hot spots. The latter is based on a direct charge transfer between an analyte molecule and substrate surface [4,5]. For organic molecule detection, the generation and intensity of the Raman signals are primarily determined by the composition and geometry of the substrates, including the shape, particle size, and interparticle gaps [6]. Thus, the active substrates play an important role in obtaining highly efficient SERS signals. Among various substrates, nanostructured noble metals (Ag, Au, and Pt) have been recognized as one of the promising SERS substrates due to their high enhancement factor (EF) and various morphologies [7–10]. Nevertheless, some metal substrates have insurmountable defects, such as high cost, poor reproducibility, low stability, and weak biocompatibility, limiting their further application. Therefore, it is a challenge to develop easy, fast, and cost-effective routes for obtaining a novel SERS substrate in the future.

Recently, it has been reported that semiconductor materials such as $TiO_2$, ZnO, ZnS, and CuTe can generate weak Raman signals (EF, $10–10^3$) [11–14]. Especially, for noble metals with $TiO_2$ nanostructure arrays, it can remarkably improve the sensitivity and reproducibility of the SERS substrate [15]. The well-controlled $TiO_2$ nanostructure arrays can be used as a feasible support structure for loading noble metal nanoparticles (NPs), preventing aggregation of noble metals. Also, an additional CM of the semiconductor/metal interface would be beneficial for improving SERS intensity and sensitivity [16]. Moreover, $TiO_2$ nanostructures have been extensively used as photocatalysts to degrade various organic molecules due to their good stability, high photosensitivity, non-toxicity, and excellent photocatalytic activity [17–20]. Hence, it is believed that noble metal/$TiO_2$ composites possess

* Corresponding author.
*E-mail address:* szq@ahu.edu.cn (Z. Sun).

https://doi.org/10.1016/j.apcatb.2019.03.084
Received 30 January 2019; Received in revised form 22 March 2019; Accepted 31 March 2019
Available online 04 April 2019
0926-3373/ 

photocatalytic performance in addition to SERS performance. After SERS detection, the active substrate can effectively degrade organic molecules adsorbed on the surface via a photocatalytic reaction, and then the substrate can be reused for SERS detection.

In addition to composition and morphology, the intensity of SERS signals also depends on the amount of adsorbed molecules on the substrates. In general, SERS signals can be detected when the target molecules are adsorbed on the surface of substrates. Weak adsorption between molecules and substrates usually results in low electromagnetic enhancement and low charge transfer. For this reason, there is a high demand to improve the adsorption capacity of molecules to enhance intensity and sensitivity of the SERS substrate. Graphene oxide (GO) has been reported to be an excellent candidate for plasmonic coupling. As a two-dimensional carbon network structure, GO contains various functional groups on the graphite plane and sheet edge, including hydroxyl, epoxy, and carboxylic acid groups [21–23]. It is easy for these polar groups to absorb polar molecules and form GO-embedded compounds. GO can adsorb a wide variety of organic molecules through electrostatic interaction and π-π accumulation due to its large π-conjugated system and high surface area [24]. Additionally, GO can offer a CT mechanism that increases the Raman signals of adsorbed target molecules [25]. Therefore, GO with these excellent properties could be combined easily with noble metal NPs to obtain a higher EF for SERS detection. For example, Hao et al. [26] fabricated a kind of Au/GO/cicada wing as a SERS substrate to detect rhodamine 6 G (R6 G), which showed a higher EF of $1.08 \times 10^6$ and a lower detection limit of $10^{-8}$ M. Lu et al. [27] adopted Au or Ag NPs to modify reduced graphene oxide (rGO), and the detection limit was as low as $10^{-9}$ M for the MB and R6 G molecules.

In this study, a novel Ag/graphene oxide/$TiO_2$ nanorod array (Ag/GO/TNR) film was designed as a photocatalyst and a recyclable SERS-active substrate by using GO as an interlayer of $TiO_2$ nanorod array and Ag NPs. This will improve the adsorption capacity and detection intensity for organic molecules. The preparation procedure for the Ag/GO/TNR substrate is shown in Scheme 1. Using R6 G as probe molecules, the adsorption capability, SERS activity, and photocatalytic property of the Ag/GO/TNR substrate were investigated. It was found that the strategy that uses a GO interlayer with suitable content to increase the adsorption capacity, signal intensity, and uniformity of the SERS substrate was indeed effective. TNR with a high photocatalytic activity effectively decomposed R6G molecules adsorbed on the surface, which was beneficial for the reusability of the SERS substrate. Furthermore, Ag NPs decorated on the GO/TNR not only increased the photocatalytic ability of the TNR due to its high surface plasma resonance (SPR) but also could be reserved as SERS-active material owing to the EM mechanism.

## 2. Experimental

### 2.1. Synthesis of Ag/GO/TNR films

The Ag/GO/TNR film was prepared using a three-step method. First, the TNR film was fabricated using a simple hydrothermal method [28]. A total of 15 mL of hydrochloric acid and 0.5 mL of $C_{16}H_{36}O_4Ti$ (TBT) were added to 15 mL of deionized water and stirred. It was then transferred to a Teflon-lined autoclave (50 mL). A pre-cleaned glass with F-doped $SnO_2$ thin film (FTO) as a substrate was placed on the bottle of the above mixture and heated at 150 °C for 10 h to form the $TO_2$ nanorod array. Next, according to our previous study, GO was synthesized using a modified Hummers' method [29]. The as-obtained GO powder was dispersed in the phosphate solution, and a uniform GO electrolyte (0.5 g/L) was formed using an ultrasonic treatment for 2 h. Then, the GO was electrodeposited on the TNR film using a standard three-electrode system. The TNR film (working electrode), Pt foil, (counter electrode), and Ag/AgCl (reference electrode) were used in the electrochemical reaction. After a deposition time of 5 min, the GO/TNR film was subsequently obtained by washing several times with deionized water. The GO/TNR film was then immersed in 0.12 M of $AgNO_3$ solution under mercury lamp (15 W) irradiation for 30 min to yield the Ag/GO/TNR film. For comparison, the Ag/TNR film was fabricated using a similar process in the absence of the GO interlayer. In addition, by adjusting the electro-deposition time from 3 min to 15 min, the GO/TNR and Ag/GO/TNR films were obtained to find the optimal deposition time of GO.

### 2.2. Characterizations

The microstructures of films were characterized with an X-ray diffractometer (XRD, M18XHF) with Cu Kα radiation (λ = 0.154178 nm). The morphologies were analyzed using a field emission scanning electron microscopy (FE-SEM, Hitachi-S4800), a transmission electron microscope (TEM, JEM-2100) and the attached energy dispersive X-ray (EDX) spectroscopy. The surface composition was recorded by an X-ray photoelectron spectrophotometer (XPS, ESCALAB-250). The absorption measurement was studied by an ultraviolet-visible (UV–vis) spectrophotometer (Shimadzu, UV-2550). Raman spectra were measured using a Renishaw Laser Micro-Raman Spectrometer (inVia) with a 532 nm laser source.

### 2.3. Adsorption capacity

R6 G was used as organic dye for the adsorption property of substrates. Each film (about $1 \times 1$ $cm^2$) was immersed in a R6 G aqueous solution (100 mL, $1 \times 10^{-5}$ mol/L). After immersing for 2 h in dark, the

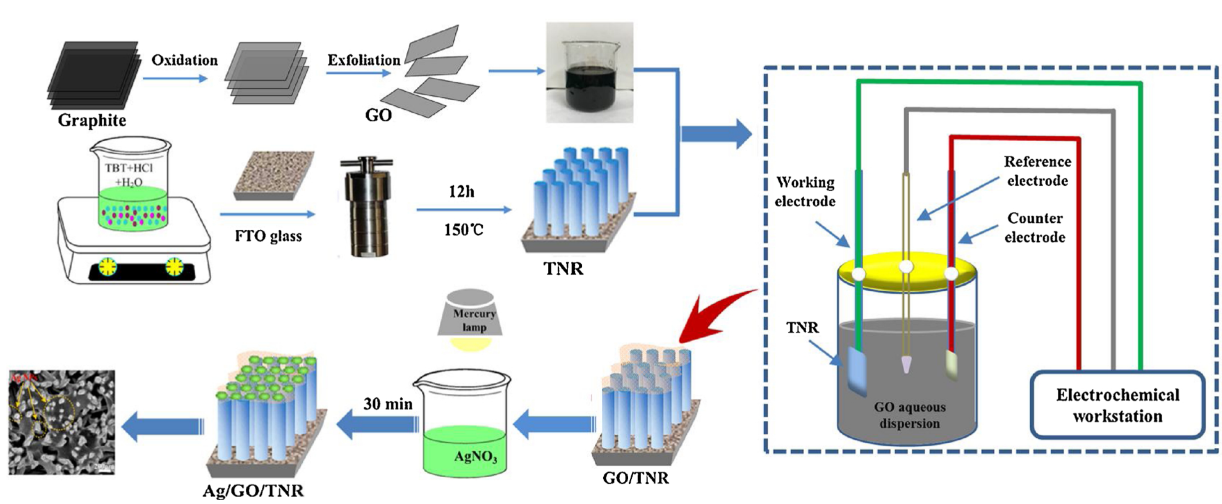


**Scheme 1.** Fabrication procedure of Ag/GO/TNR substrate.

sample was taken out and used to analyze adsorption capacity using UV–vis spectrophotometer. The absorption ratio was calculated by Eq. (1):

$$C = \frac{C_0 - C_t}{C_0} \tag{1}$$

Where $C_0$ is the initial concentration, $C_t$ is the absorbance concentration after 2 h.

### 2.4. SERS property

SERS properties of substrates were tested by R6 G as probe molecules. The analytes with various concentrations were prepared by diluting R6 G with distilled water. Then, the as-prepared samples as substrates were immersed to the R6 G solution ($10^{-5}$–$10^{-12}$ M). After for 30 min, the substrates were cleaned by distilled water and blown by nitrogen. Finally, the substrates were used for the analysis of SERS properties using a Micro-Raman Spectrometer.

### 2.5. Recycle stability

To further evaluate the recyclability of substrate, the Ag/GO/TNR immersed in distilled water was irradiated under a Xenon lamp (150 W). Because of the photocatalytic activity, this process can lead to the degradation of R6 G molecules adsorbed on the surface of substrate. After 60 min, the substrate was cleaned with distilled water several times, and it was again used for SERS test. The total experiment procedure is shown in Scheme 2. The above experiment was repeated three times to illustrate recyclable property.

### 2.6. Photocatalytic property

The photocatalytic properties of substrates were evaluated by the degradation of R6 G under simulated sunlight irradiation, which was from a Xenon lamp (150 W). In each test, the substrate (about $1 \times 1$ cm$^2$) was immersed in a rectangular beaker containing a R6 G solution (10 mL, $10^{-6}$ M). Before the light was turned on, the solution was kept in dark for 60 min for achieving an adsorption and desorption equilibrium. The distance between lamp and substrate was 10 cm. The catalytic efficiency of R6 G was determined by UV–vis absorption intensity at 522 nm.

## 3. Results and discussion

### 3.1. Structure and morphology analysis

Fig. 1 shows the XRD patterns of the GO, TNR, GO/TNR, and Ag/GO/TNR samples. In Fig. 1(a), the characteristic peak of GO is 10.15°. The diffraction peaks of the TNR, GO/TNR, and Ag/GO/TNR show similar indexing patterns [see Fig. 1(b)]. Four main diffraction peaks appear at 2θ = 36.10°, 54.47°, 62.74°, and 69.79° that are assigned to the (101), (211), (002), and (112) planes of the rutile phase $TiO_2$ (JCPDS no. 21–1276). Nevertheless, the diffraction peaks of GO and metallic Ag cannot be detected in the XRD patterns, primarily due to the strong diffraction from rutile $TiO_2$ and small amounts of GO and Ag NPs.

Fig. 2 reveals the SEM images of the different samples. An analysis of the SEM [see Fig. 2(a)] and TEM images [see Fig. 2(b)] of the GO shows that the morphology of GO appears in a wrinkled and expanded layer structure, which is a typical feature of sheet-like GO. Such a GO with a large specific surface area is very beneficial for an intermediate layer of Ag and $TiO_2$ to obtain good adsorption capability. Fig. 2(c) and (d) show a cross-section view and top view of the TNR. The $TiO_2$ product displays a highly ordered and vertically aligned nanorod array structure, with a rod diameter of approximately 100 nm and a rod length of approximately 2.4 μm. The length and diameter of the nanorods rely on reactive temperature, time, PH, precursor concentration, and other experimental parameters. After the electrochemical deposition of GO, many flaky coatings attached to the surface of TNR can be observed in Fig. 2(e), while the characteristic of the $TiO_2$ nanorod array is still maintained. Furthermore, compared with the rough top of the single nanorod, the top edges of $TiO_2$ are also coated with a thin film and become relatively smoother for the GO/TNR, which could be due to the deposition of GO. It has been demonstrated that a GO/TNR substrate immersed in an $AgNO_3$ solution may produce abundant electron-hole pairs due to electron transition under UV irradiation. Interestingly, these charge carriers would move to the surface and undergo first a reduction reaction and then oxidation. According to this principle, Ag

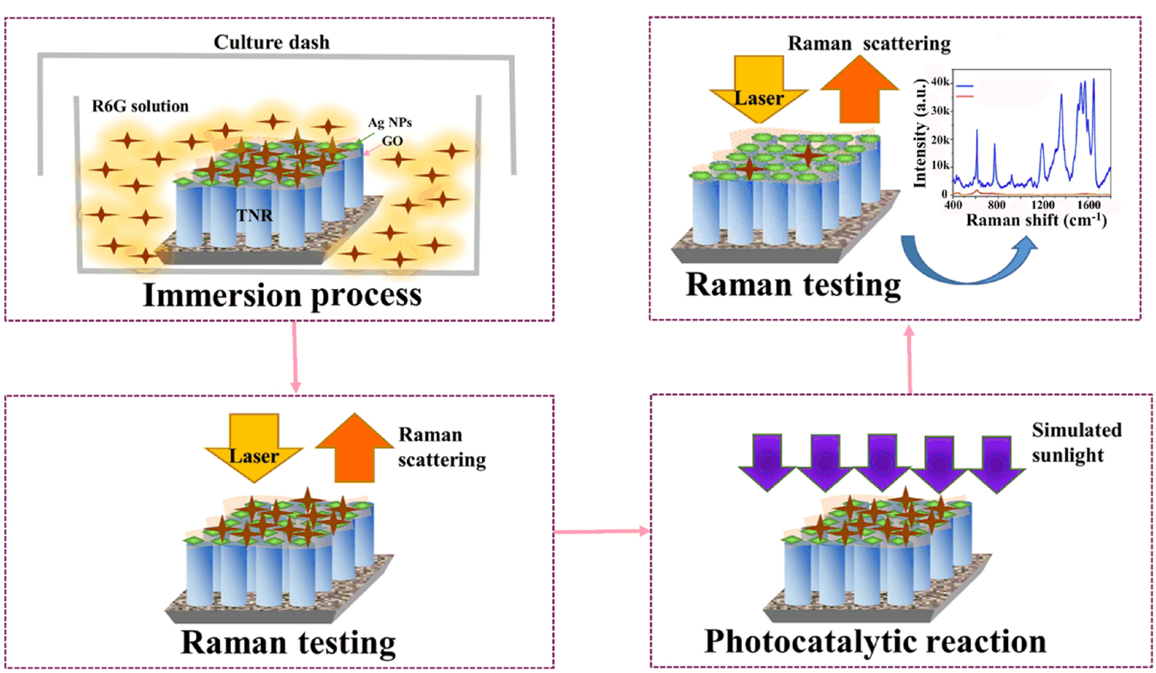


**Scheme 2.** Photocatalytic test process of Ag/GO/TNR substrate for R6 G.

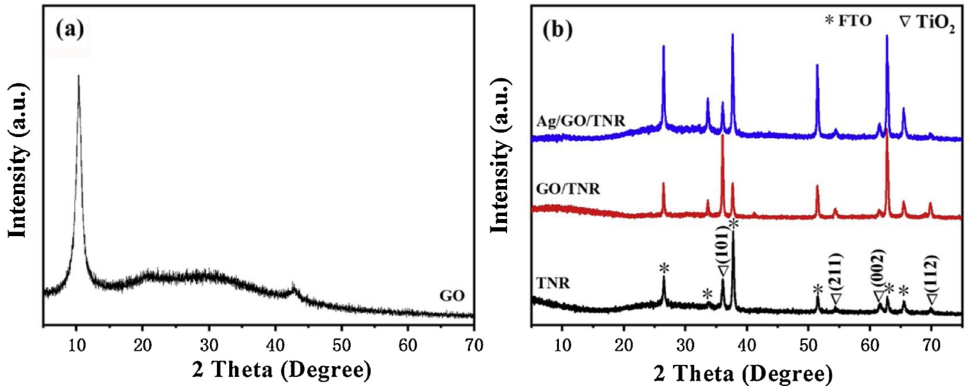


**Fig. 1.** XRD patterns of the samples: (a) GO, (b) TNR, GO/TNR, and Ag/GO/TNR.

species would therefore be photo-reduced on the surface of the GO/TNR. As shown in Fig. 2(f) Ag nanoparticles (NPs) are homogeneously deposited on the GO surface. The Ag NPs are approximately 20–50 nm in diameter, suggesting that Ag NPs have a relatively wide size distribution. In addition, some Ag particles aggregate with each other in pairs, forming many dimers on the surface of the GO/TNR. Most importantly, the surfaces of the Ag NPs deposited on the GO/TNR are relatively rough, and there are many points that have a large curvature. The distance between the adjacent particles is less than 50 nm, which will benefit the enhancement of the local electric field on the surface of the substrate [30]. Fig. 2(g) shows the optical photographs of the TNR, GO/TNR, and Ag/GO/TNR samples. With the successive deposition of GO and Ag NPs, the color of the substrate gradually deepens from a semitransparent white to dark and then to black. Thus, these phenomena confirm that the GO nanosheets and the Ag NPs are successively loaded on the TNR surface.

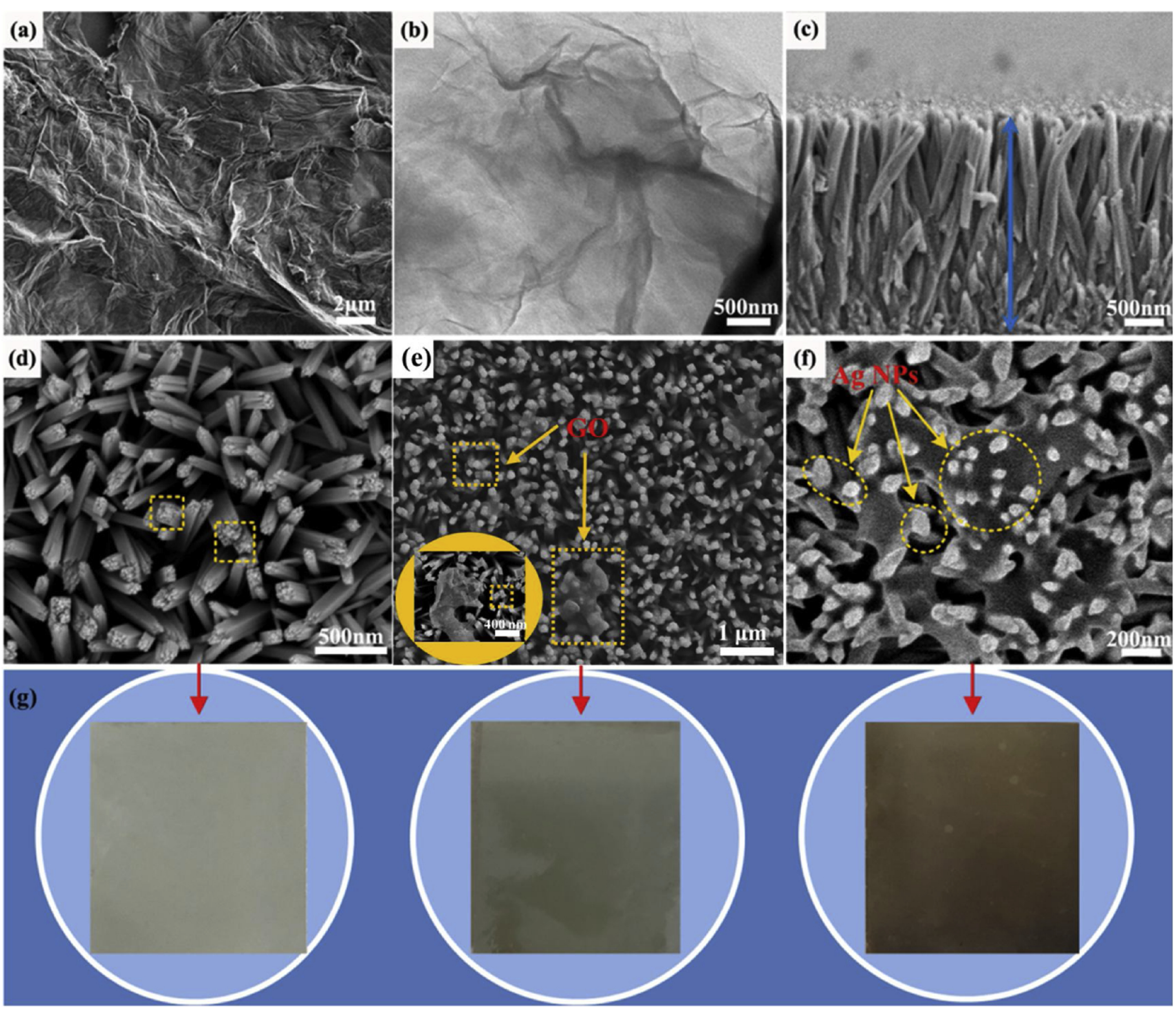


**Fig. 2.** SEM images of the samples: (a) GO, (c) cross-section view and (d) top view of TNR, (e) GO/TNR (Inset: FESEM), (f) Ag/GO/TNR; (b) TEM image of GO; (g) the responding photographs.

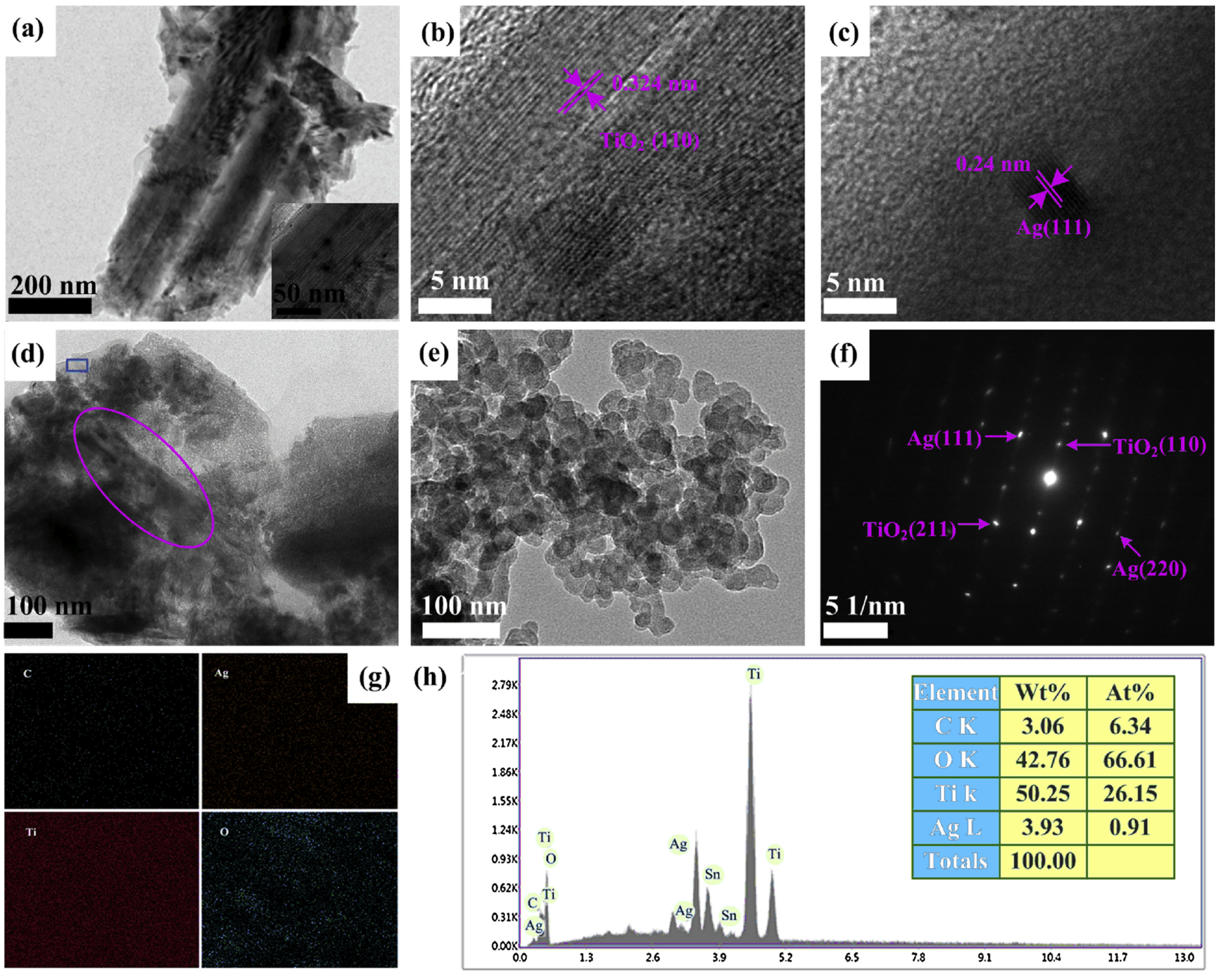


**Fig. 3.** (a) TEM and (b, c) HRTEM images of Ag/TNR, (d, e) TEM images of Ag/GO/TNR sample, (f) the SAED patterns of Ag NP and $TiO_2$ nnaorod, (g) element mapping and (h) EDX analysis of Ag/GO/TNR substrate.

The microstructure and morphology of the TNR substrate decorated with Ag NPs were analyzed for comparative analysis. Fig. S1 shows the XRD pattern of the as-prepared Ag/TNR, which is basically the same as that of pure TNR [see Fig. 1(b)]. Four characteristic diffraction peaks from the rutile phase $TiO_2$ can be clearly observed, but metallic Ag cannot be detected. The TEM and HRTEM images in Fig. 3(a) further indicate that the Ag NPs tightly grow on the surface of the TNR. The HRTEM images in Fig. 3(b) and (c) show two kinds of lattice fringes. The 0.324 nm corresponds to the interlayer spacing of the (110) plane of the rutile $TiO_2$, and 0.24 nm relates to the (111) plane of the face-centered cubic Ag. Fig. S2 shows a picture of the Ag/TNR sample. Analogously, due to the deposition of Ag particles, the surface of the Ag/TNR substrate turns from semitransparent white to black compared with the pure TNR. Furthermore, the detailed morphology of the Ag/GO/TNR substrate was analyzed using TEM and HRTEM. Fig. 3(d) shows the wrinkled GO is marked with a blue rectangular box, and a $TiO_2$ nanorod is marked with a red oval. The diameter of the $TiO_2$ nanorod is approximately 100 nm, which is in accordance with the result of the SEM images (see Fig. 2). Additionally, a large number of Ag NPs can be clearly observed, as shown in Fig. 3(e). Fig. 3(f) shows the SAED pattern of the Ag NP and $TiO_2$ nanorod, which demonstrates single crystalline features. In addition, the element mapping [see Fig. 3(g)] of C, Ag, Ti, and O also reveals the co-presence of GO and Ag NPs on the TNR structure. According to the EDX analysis in Fig. 3(h), the weight ratio of C, O, Ti, and Ag is determined to be 3.06%, 42.76%, 50.258%, and 3.93%, respectively.

### 3.2. XPS analysis

XPS was performed to investigate the chemical states of the Ag/GO/TNR substrate. For comparison, the XPS spectra of the TNR and the GO/TNR were also analyzed. As shown in Fig. 4(a), Ag, O, Ti, and C in the Ag/GO/TNR and O, Ti, and C in the GO/TNR can be clearly observed in the survey spectra. For the TNR, the existence of the C element may come from foreign pollution of carbon. The O 1 s spectra can be deconvoluted into two peaks, as shown in Fig. 4(b). For the TNR, the two peaks at 531.6 eV and 530.1 eV are associated with the Ti−O−H and Ti−O groups, respectively [31]. However, for the GO/TNR and Ag/GO/TNR, a new peak located at 532.5 eV can be assigned to the C−O groups [32], which is closely related to the existence of GO. Fig. 4(c) shows the high-resolution XPS spectra of Ti 2p. Compared with the TNR that has binding energies of 464.6 eV and 458.8 eV, those in the Ag/GO/TNR are located at 464.9 eV and 461.1 eV. This suggests the existence of the $Ti^{4+}$ state in the samples, and a slight shift of 0.3 eV indicates the interaction between GO and rutile $TiO_2$ [33]. Fig. 4(d) shows the C 1 s spectra of GO/TNR and Ag/GO/TNR. By deconvolution, three obvious peaks can be ascribed to those of C=C−O−H/C−O−C (286.5 eV), and Ti−O−C/O−C=O (288.6 eV) [34]. This result further confirms the existence of GO, which agrees well with the EDX result. For the Ag/GO/TNR substrate, two characteristic peaks of 374.4 eV and 368.3 eV can be observed in Fig. 4(e) that correspond to Ag $3d_{5/2}$ and Ag $3d_{3/2}$ in metallic Ag [35]. These findings further suggest that the Ag NPs have been successfully deposited on the GO nanosheets to form the Ag/GO/TNR active substrate.

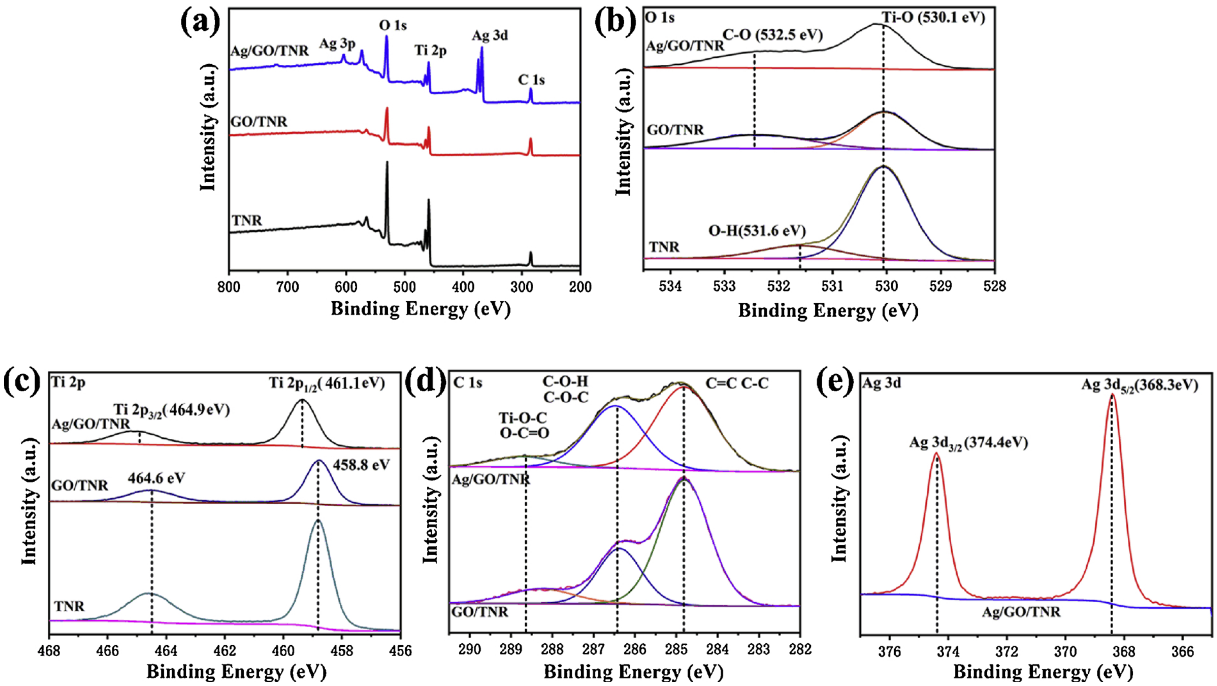


**Fig. 4.** XPS spectra of the as-prepared samples: (a) survey, (b) O 1 s, (c) Ti 2p, (d) C 1s, (e) Ag 3d.

### 3.3. Optical property

The UV–vis absorption spectra of the TNR, GO, Ag/TNR, GO/TNR, and Ag/GO/TNR samples are shown in Fig. 5(a). It can be seen that the characteristic peak of GO is located at 320.1 nm, which is related to the absorption of the C═O bond [36]. The TNR possesses a strong absorption in the ultraviolet region, in agreement with the band energy of rutile $TiO_2$ [37]. For the Ag/TNR film, in addition to a strong UV light absorption of $TiO_2$, an obvious visible light absorption from 450 nm to 700 nm can be observed owing to the SPR absorption of metal Ag NPs. There are two conspicuous absorption edges in the spectra of the GO/TNR and the Ag/GO/TNR. These can be attributed to the characteristic absorptions of GO and $TiO_2$. This confirms that the GO nanosheets and $TiO_2$ nanorods are present in the sample. Compared with the GO/TNR, a red shift of the absorption edge can be obviously observed for the Ag/GO/TNR. Additionally, the Ag/GO/TNR film shows prominent surface plasmon absorption in the range of 450–700 nm, confirming the presence of Ag NPs. The SPR absorption center of the Ag/GO/TNR is located at approximately 550 nm, which shows an obvious redshift compared with that of the plasmonic metal Ag NPs previously reported in the literature [38]. This phenomenon may be due to the formation of Ag dimers, as shown in the SEM images [see Fig. 2(f)]. Researches have shown that when metal nanoparticles (Au or Ag) get close to each other to form dimers, the isotropic SPR of adjacent nanoparticles will produce a coupling effect in the uniaxial direction. This can be achieved with a strong local electromagnetic field in the axis of the dimer, resulting in a redshift of SPR absorption for metal NPs [39]. Furthermore, the shape, diameter, and environment of Ag NPs also have a significant impact on the characteristic peaks of the SPR.

Theoretical analysis have revealed that the gap nature of GO is related to the oxidation level. The gap structure of GO can change from direct to indirect with the increase of oxygen functional groups, due to the change of highest valence band from the π orbital to the O 2p orbital [40–45]. In the system, the bandgap energies of the films are determined using the plots of $(\alpha h\nu)^2$ versus photon energy ($h\nu$) for the direct gap. GO is a noncrystal that is composed of graphene molecules with different oxidation levels, so a sharp adsorption edge with precise bandgap energy cannot be observed in the convert plots [46]. By the approximate linear extrapolation, the apparent bandgap of 3.02, 2.56, 2.93 and 2.46 eV are obtained for TNR, GO/TNR, Ag/TNR, and Ag/GO/TNR, respectively (Fig. 5b). The narrow bandgap suggests that the deposition of Ag NPs and GO interlayer on the TNR films can significantly increase the sunlight absorption, leading to the improved photocatalytic activity.

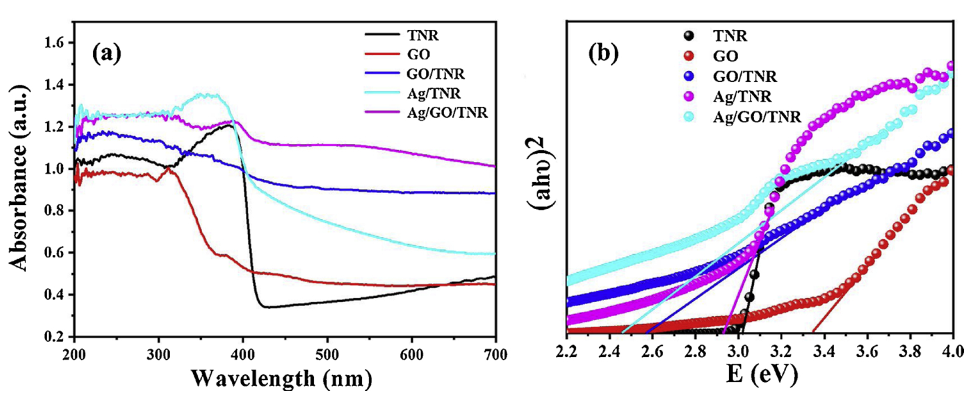


**Fig. 5.** (a) UV–vis absorbance spectra and (b) the determination of the absorption edges of the samples.

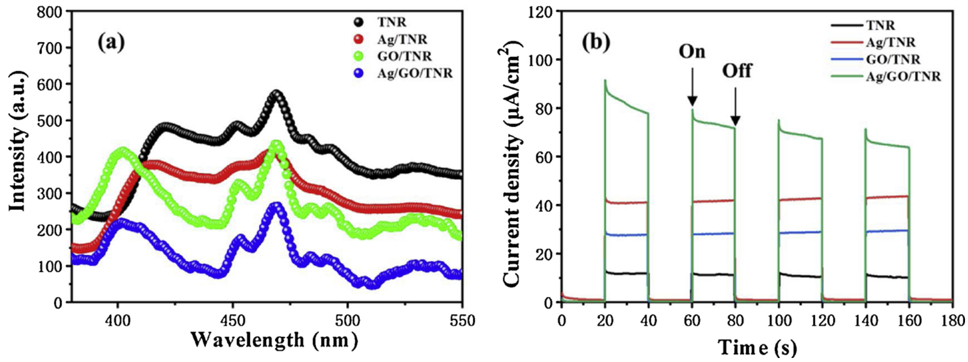


**Fig. 6.** (a) PL spectra and (b) transient photocurrent responses of TNR, Ag/TNR, GO/TNR and Ag/GO/TNR films.

### 3.4. PL spectra and photoresponse

In order to further study the separation, recombination and transfer of photo-generated charge carriers, PL spectra of the different films are shown in Fig. 6(a). All of films mainly emit five PL peaks, which are located at 420, 452, 469, 484, and 493 nm, respectively. They can be contributed to intrinsic emission or emission from exciton and defect. Compared with TNR, the binary Ag/TNR and GO/TNR films show an obvious decrease in the PL intensity. This is because the charge carriers are captured and transferred by Ag 3d energy level and GO as an electron acceptor, respectively, efficiently inhabiting the recombination of photo-generated electrons and holes [47,48]. Moreover, the PL intensity of Ag/GO/TNR film is much lower than the single film and binary films, indicating a lower electron-hole recombination rate. It suggests that the synergistic effect of Ag NPs and GO interlayer on TNR is beneficial to facilitating the transport and transfer of photo-generated charge carriers.

In addition, the photoresponse property of electrodes was carried out under simulated sunlight illumination with 20 s intermittent on-off. Fig. 6(b) shows the photocurrent-time characteristics of TNR, Ag/TNR, GO/TNR and Ag/GO/TNR films. It is obvious that all of photoanodes possess a rapid and good photoresponse. The photocurrent density is almost negligible in the dark condition, while the current density quickly increases after the intermittent light is turned on. Due to the trapping of photo-generated charges, the current rapidly decreases to a stable value of 77.9 $\mu A/cm^2$. More importantly, the current density of Ag/GO/TNR photoanode is about 6 and 2.9 times higher than that of TNR and Ag/TNR, respectively. The result indicates that the photo-generated electrons are efficiently separated from holes in the Ag/GO/TNR film, resulting in an improved catalytic activity.

### 3.5. Adsorption capability

To investigate the effect of GO on the adsorption capability of the substrates, the TNR, Ag/TNR, GO/TNR, and Ag/GO/TNR samples were immersed in an R6 G solution for 2 h in the dark. Fig. 7(a) shows the UV–vis spectra of the different samples in the R6 G solution after adsorption for 2 h. A significant decrease in the characteristic absorption (522 nm) can be observed, and the four substrates display different adsorption effects. Fig. 7(b) presents the adsorption ratios of R6 G for the different substrates. The adsorption ratio of R6 G for the TNR and Ag/TNR is approximately 16% and 38% at 2 h, respectively. This result indicates that the adsorption capacity of the Ag/TNR is higher than that of the TNR. This is because the covalent bonding between the R6 G molecules and the Ag NPs helps to improve the adsorption capability of the Ag/TNR. The adsorption effect of the GO/TNR is similar to that of the Ag/TNR. Furthermore, the Ag/GO/TNR substrate shows the highest adsorption ratio at 44%. This is because GO has abundant oxygen-containing functional groups, and a highly negative charge can interact with the positive charged R6 G molecules through an electrostatic interaction. Moreover, GO nanosheets with aromatic domains may form π-π stacking with π-electron-rich R6 G. In addition, $N_2$ adsorption-desorption isotherm was used to characterize surface area of Ag/GO/TNR film, as shown in Fig. S3. Based on the multi-point Brunauer-Emmett-Teller (BET) method, the specific surface area of Ag/GO/TNR is calculated to be 392.402 $m^2\,g^{-1}$. This value is obviously higher than the surface areas of the reported $TiO_2$ nanoarray films, such as $TiO_2$ nanorod (78 $m^2\,g^{-1}$), $TiO_2$ nanotube (245 $m^2\,g^{-1}$) and hierarchical anatase/rutile $TiO_2$ photoanode (375 $m^2\,g^{-1}$) [49–51]. These findings suggest that the higher adsorption capability and larger surface area of the Ag/GO/TNR will be beneficial for photocatalysis and SERS performance.

### 3.6. SERS performance

To study the effect of the GO interlayer on the substrate, the UV–vis spectra of the Ag/GO/TNR films obtained using different GO deposition times are shown in Fig. S4(a). In the spectra of the Ag/GO/TNR films, the optical response range is extended to the visible light region. Three significant absorption edges are attributed to the characteristic absorption of Ag NPs, GO, and the $TiO_2$ component. It is worthwhile to note that with the extended deposition time, there is an increase in the characteristic absorption of GO. To further observe this phenomenon, the morphologies of the GO/TNR obtained at various GO deposition times are shown in Fig. S4(b)–(d). With increasing deposition time, the structure of the TNR does not change significantly, but the surface modification and coverage of GO on the TNR gradually increase. When the deposition time is 15 min, the surface of the TNR substrate becomes covered with numerous GO nanosheets, even forming multilayer stacking. However, too many GO interlayers may reduce the adsorption capacity and subsequent uniform deposition of Ag NPs.

The SERS activity of the TNR, Ag/TNR, GO/TNR, and Ag/GO/TNR substrates with different GO was evaluated using R6 G probe molecules. Fig. 8(a) shows the SERS spectra of the R6 G adsorbed on the substrates using a $1 \times 10^{-6}$ M aqueous solution. It can be seen that the R6 G molecule has eight Raman peaks centered at 611, 773, 1181, 1309, 1362, 1506, 1574 and 1649 $cm^{-1}$ that might be due to the vibration modes of the groups, such as a C–C–C ring, C–H, and aromatic C–C [52]. Except for the diffraction peaks of $TiO_2$ and GO, no other peaks from R6 G can be observed in the GO/TNR substrate. It is evident that the Ag/GO/TNR substrates show significant enhanced SERS intensity compared with the Ag/TNR. In addition, there is an obvious difference in the signal intensity for the Ag/GO/TNR substrates with different GO deposition times. When the deposition time of GO is 5 min, the Ag/GO/TNR substrate achieves the highest SERS signals. Fig. 8(b) shows the SERS intensity at 1650 $cm^{-1}$ of the substrates. It reveals that GO nanosheets as interlayers have a significant effect on the sensitivity improvement of the substrates. The interpretations for the highest SERS signals of the Ag/GO/TNR-5 min can be explained as follows. First, a substrate with a higher adsorption capacity absorbs more probe

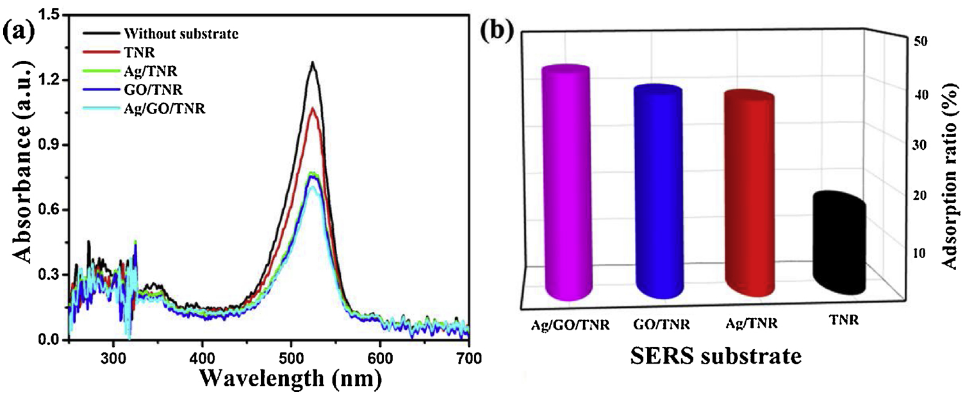


**Fig. 7.** (a) UV–vis absorption spectra and (b) adsorption ratio of the different substrates for R6 G solution ($1 \times 10^{-5}$ M) after 2 h.

molecules, which leads to an increase in the SERS sensitivity. Alternately, homogeneous Ag NPs decorated on the GO/TNR surface may provide a pretty rough structure and appropriate interparticle gap that would produce higher density hotspots. Also, the EM mechanism of the Ag NPs helps improve the SERS intensity and uniformity of the substrate. Additionally, the charge transfer between GO and R6 G assists the chemical mechanism, and this would enhance the Raman signals. Therefore, the SERS performance of the substrate is significantly improved due to the synergistic effect of the Ag NPs, GO nanosheets, and $TiO_2$ nanorod array.

Based on the above result, the Ag/GO/TNR sample obtained with a 5 min deposition time of GO was used for the following analysis. Fig. 9(a) shows the SERS spectra of R6 G with different concentrations adsorbed on the Ag/GO/TNR substrates. The Raman signals of the substrate gradually reduce along with an increase in dilution times. It should be noted that the Raman signals of R6 G can still be well observed even at $1.0 \times 10^{-12}$ M. It means that the detection limit of R6 G can reach as low as $10^{-12}$ M for the Ag/GO/TNR substrate, indicating a high SERS sensitivity. Fig. 9(b) shows the relationship between the R6 G concentration and the Raman intensity located at 1650 $cm^{-1}$. It can be seen that the Raman signal gradually weakens with a decreasing R6 G concentration. Using logarithmic transformation, the relationship between log $C$ (logarithmic concentration) and log $I$ (logarithmic intensity) appears as an approximate linear relationship in the inset. This result conforms to the Langmuir adsorption isotherm of the analyte molecule [53]. In addition, this linear relationship could provide an experimental foundation for the substrate calibration and concentration measurement of R6 G molecules.

The SERS sensitivity of the Ag/GO/TNR substrate is evaluated using the apparent enhancement factor (EF) [42]:

$$EF = I_{SERS} N_{solid} / I_{solid} N_{SERS} \tag{2}$$

where $I_{SERS}$ and $I_{solid}$ are the SERS intensity of R6 G on the Ag/GO/TNR substrate (1560 $cm^{-1}$, $1.0 \times 10^{-6}$ M) and the glass substrate (1560 $cm^{-1}$, solid R6 G), respectively. $N_{SERS}$ and $N_{solid}$ are the corresponding molecule numbers in the laser spot area. The molecules are assumed to have a monolayer distribution on the substrates, and the molecule numbers can be evaluated using the equation:

$$N_{SERS} = (N_A CV / S_{sub}) S_{laser} \tag{3}$$

where $N_A$ is the Avogadro constant; $C$ is the R6 G concentration of $1.0 \times 10^{-6}$ M; $V$ is the droplet volume of 2 µL; $N_{sub}$ is the solution dispersed area on a substrate of 5 mm; and $N_{laser}$ is the laser spot diameter of 1 µm. The probe molecule numbers on a solid substrate can be calculated using the following equation:

$$N_{Solid} = S_{laser} d \rho N_A / M \tag{4}$$

where $d$ is the penetration depth of 2 µm; ρ is the density of 0.79 $g/cm^3$; and $M$ is the molar mass of 479 g/mol. According to the above equations, $N_{solid} / N_{SERS}$ is calculated to be $4.82 \times 10^4$. In addition, $I_{SERS} / I_{solid}$ is calculated to be 12.16 according to the SERS spectra of R6 G on the Ag/GO/TNR and glass substrate [see Fig. 9(c)]. Thus, the EF is estimated to be approximately $5.86 \times 10^5$. The high EF value suggests that the Ag/GO/TNR substrate has a remarkable Raman enhancement effect for R6 G detection [54].

It has been demonstrated that the uniformity of Raman signals is a critical property for a SERS substrate. A large area of GO interlayer covered on a high-ordered $TiO_2$ nanorod array may offer a homogeneous platform for the deposition of Ag NPs, leading to a uniform distribution of hotspots. Fig. 10(a) shows a series of Raman spectra collected from ten different spots for R6 G. It can be observed that there is no obvious difference in the Raman intensity, indicating good reproducibility. The RSD value of the vibration at 1650 $cm^{-1}$ is calculated to be 8.71%, as shown in Fig. 10(b). Although the RSD value is higher than that of the Ag/TNR, it is still comparable with previous

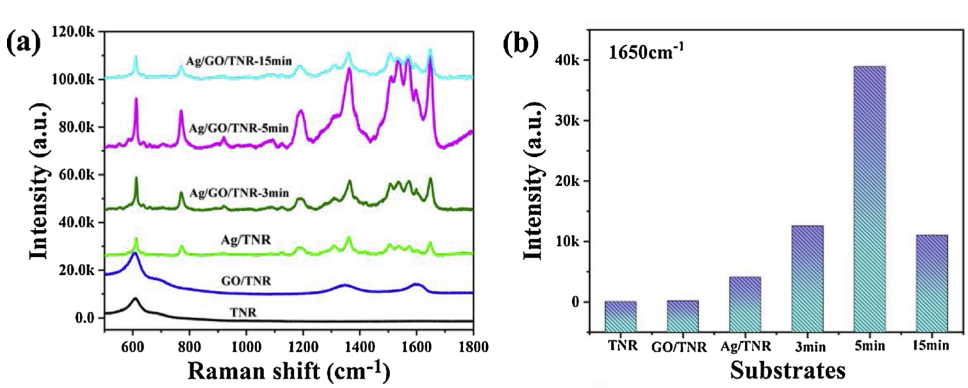


**Fig. 8.** (a) SERS spectra of R6 G adsorbed on the substrates from $1 \times 10^{-6}$ M aqueous solution, (b) SERS intensity at 1650 $cm^{-1}$ of the substrates.

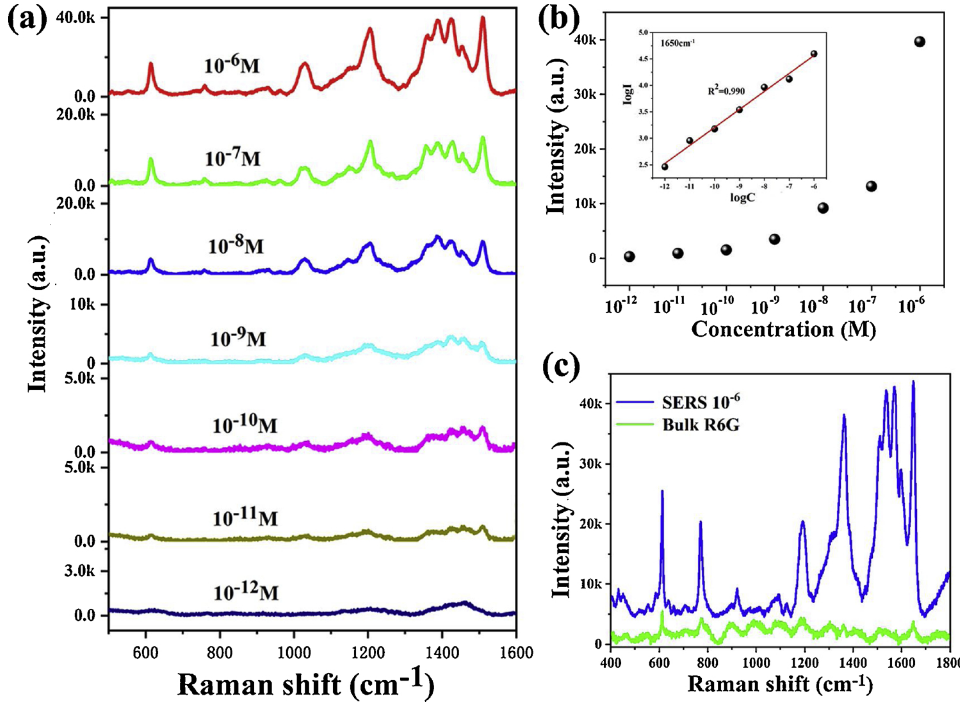


**Fig. 9.** (a) SERS spectra of R6 G with different concentrations adsorbed on Ag/GO/TNR substrates, (b) quantitative relation curve for the logarithm of the integrated SRES band at 1650 $cm^{-1}$, and (c) SERS spectra of R6 G on Ag/GO/TNR ($10^{-6}$ M) and solid R6 G on glass substrate.

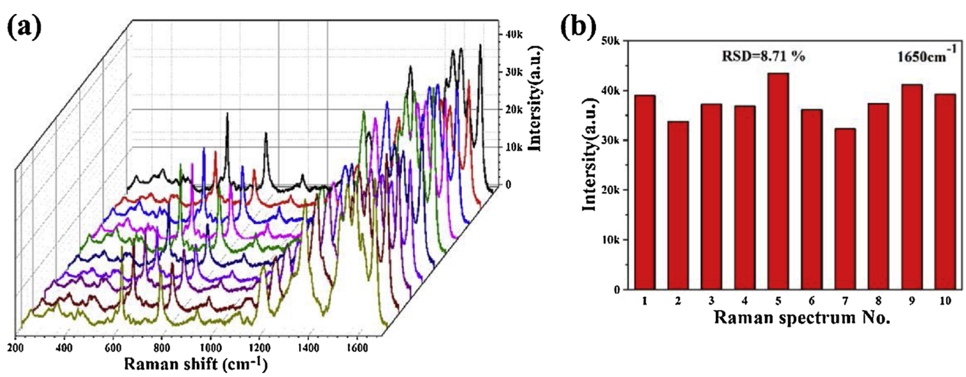


**Fig. 10.** (a) SERS spectra collected from 10 different spots for R6 G ($10^{-6}$ M) on Ag/GO/TNR substrate, and (b) the corresponding intensity of peak at 1650 $cm^{-1}$.

reports [55–57]. This result reveals that the outstanding sensitivity and good uniformity make the Ag/GO/TNR film promising as a potential SERS substrate.

Furthermore, TNR support in the Ag/GO/TNR system is expected to have a good photocatalytic ability for R6 G molecules, endowing the substrate with good reusability. Fig. 11(a) shows the SERS spectra of R6 G adsorbed on the Ag/GO/TNR before and after Xenon lamp irradiation. Obviously, all characteristic peaks of R6 G almost totally disappear when the light irradiation reaches 60 min. The photodegradation efficiency is calculated to be approximately 99.4% with a Raman intensity ratio of 1650 $cm^{-1}$. This finding proves that the Ag/GO/TNR substrate possesses an excellent self-cleaning ability. After simulated sunlight irradiation, the Ag/GO/TNR substrate was once again used in SERS detection, and the characteristic intensity was nearly unchanged. Over three recycles, the substrate maintains excellent Raman signals [see Fig. 11(b)]. This suggests that the Ag/GO/TNR substrate possesses good reusability and can be recycled for SERS detection. In addition, the morphology of Ag/GO/TNR substrate after cycle was tested, as shown in Fig. 11(c). From the SEM image, we can see that a large number of Ag NPs are still uniformly dispersed on the surface of GO interlayer. In addition to the agglomeration or larger size of individual nanoparticles, most Ag NPs remain the same size and morphology. Many dimers can be still observed and they keep the proper spacing, which generates a lot of hotspots and enhances local electric field. Thus, the intensity of Raman signals can remain good stability in the cycle test.

### 3.7. Photocatalytic analysis

In order to further study photocatalytic property, a catalytic experiment was performed by the degradation of R6 G, where a 150 W Xenon lamp was used as the simulated sunlight source. Fig. 12 (a–c) show the UV–vis spectra of R6 G solution with TNR, Ag/TNR, and Ag/GO/TNR films under the simulated sunlight for various durations. With the increasing exposure time, the characteristic absorption peak of R6 G at 522 nm drastically decreases. It indicates that R6 G molecules in the solution are gradually degraded under sunlight. Fig. 12(d) shows the photodegradation curves of R6 G under the condition of different photocatalysts, where $C_0$ and $C_t$ are the initial concentration after adsorption equilibrium and reaction concentration of R6 G, respectively.

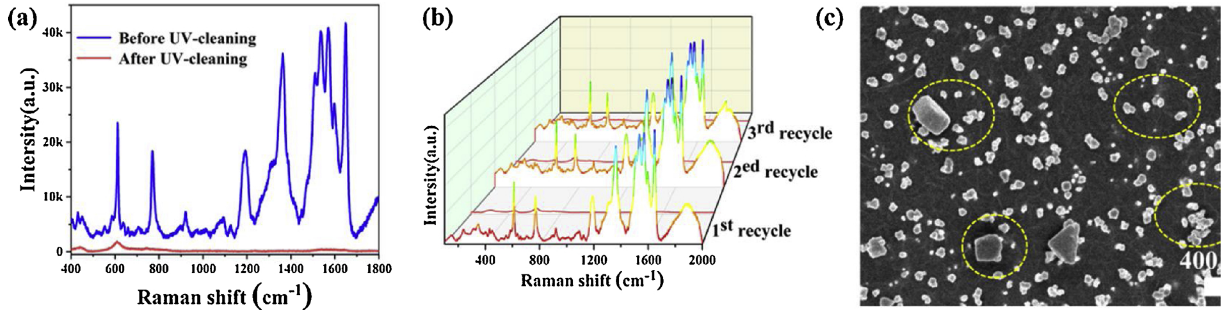


**Fig. 11.** (a) SERS spectra of R6 G solution ($10^{-6}$ M) adsorbed on Ag/GO/TNR before and after Xenon lamp irradiation, (b) recyclable SERS behavior of Ag/GO/TNR with 3 repeated treatments, and (c) SEM image of the substrate after cycle.

After 90 min of irradiation, the degradation rates are 26% and 38% by TNR and Ag/TNR film. In the presence of Ag/GO/TNR substrate, the photodegradation of R6 G reaches 66% after 90 min, which is 2.5 times higher than that of bare TNR film and up to 1.7 times for Ag/TNR film. These findings suggest that the ternary Ag/GO/TNR substrate possesses optimal photocatalytic performance, which underscores the significance of growing Ag NPs and GO interlayer on the TNR surface for capturing sunlight and promoting carrier migration. Furthermore, the inset in the Fig. 12(d) shows the approximately linear dependence between ln ($C_0$/C) and exposure time for the three substrates, and the corresponding rate constant (k) are also calculated. The k order of photocatalysts is as follows: TNR < Ag/TNR < Ag/GO/TNR. Obviously, the Ag/GO/TNR film shows a maximum k of 0.012015 $min^{-1}$, which is 3.59 and 2.3 times higher than those of TNR and Ag/TNR, respectively. These findings mean that the Ag/GO/TNR substrate has the significantly enhanced photocatalytic activity towards degradation of R6 G.

### 3.8. Photostability

The photostability of Ag/GO/TNR substrate was tested by the continuous irradiation from a simulated sunlight, as shown in Fig. 13(a). After the irradiation of 60 min, the microstructure and SERS property of the substrate were analyzed by XRD, SEM and Raman, respectively. As shown in Fig. 13(b–c), XRD characteristic peaks of the film are almost unchanged after the irradiation of simulated sunlight. Meanwhile, the size and morphology of Ag particles deposited on the GO/TNR surface do not significantly change. For the R6G molecules detection, the treated Ag/GO/TNR substrate still shows significant enhanced SERS signals. Eight Raman peaks located at 611, 773, 1181, 1309, 1362, 1506, 1574 and 1649 $cm^{-1}$ from R6G molecules can be clearly observed. These findings suggest that the Ag/GO/TNR substrate can keep good photostability under light irradiation.

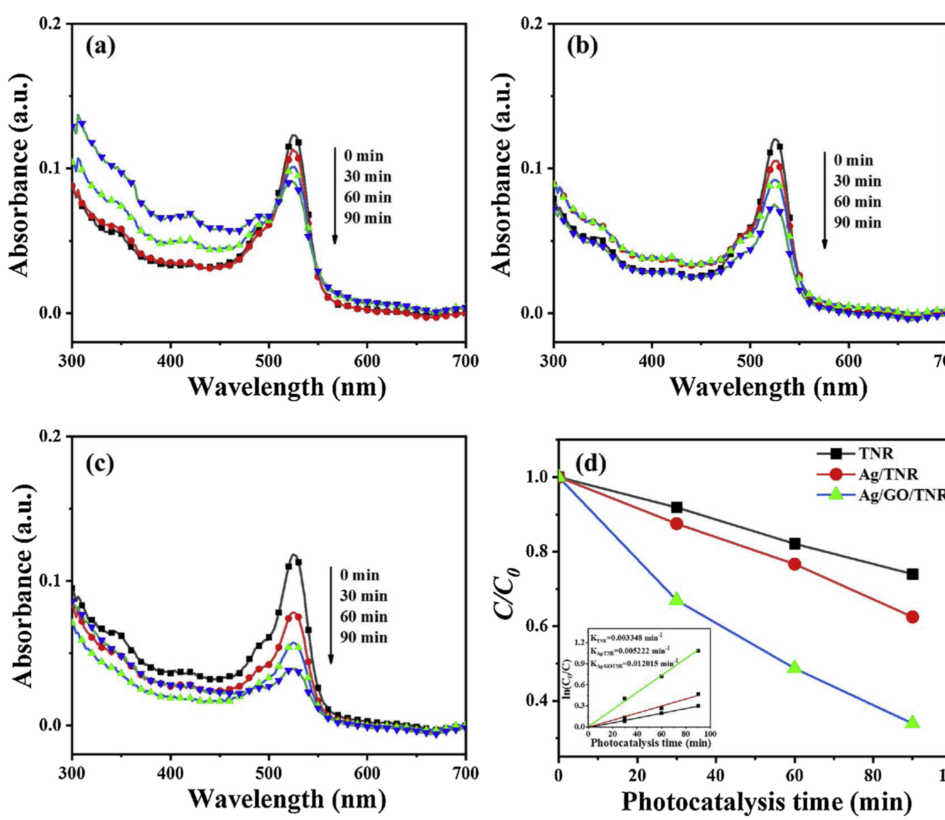


**Fig. 12.** UV–vis spectra of R6 G ($1 \times 10^{-6}$ M) by different samples under simulated sunlight: (a) TNR, (b) Ag/TNR, (c) Ag/GO/TNR, and (d) corresponding photocatalytic degradation curves (inset: kinetics and rate constant).

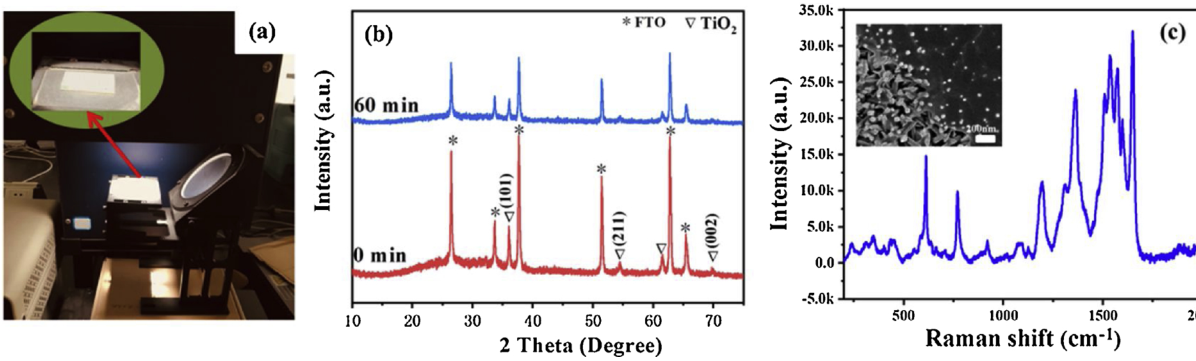


**Fig. 13.** (a) Photograph and (b) XRD pattern of Ag/GO/TNR film after 60 min irradiating time, and (c) SERS spectra of R6 G ($1 \times 10^{-6}$ M) adsorbed on the substrate (Inset: SEM image).

*3.9. Photocatalytic mechanism and SERS enhancement mechanism*

In the present system, the GO interlayer plays a key role in the improvement of photocatalytic performance and Raman signals. In general, the conductivity of GO may be poor due to its various oxygen-containing functional groups on the surface. With varying the oxidation level, the gap nature and electronic property of GO are found to be varied. This is because that the composition of the oxygen bonding can form the $sp^3$ hybridization on graphene [58–62]. The electronegativity of the oxygen atoms is larger than carbon atoms, so GO becomes a p-doped material where the charge flow produces negative oxygen atoms and carbon grid with positive charge [63–67]. As oxygen bonds on graphene increase, the valence band changes from π orbital to O 2p orbital, resulting in a larger bandgap structure of GO. Thus, the bandgap of GO can increase with increasing the oxidation level. The completely oxidized GO is an insulator, while the partially oxidized GO is a semiconductor [40,41]. Based on the above consideration, a possible photodegradation mechanism of R6G molecules on the Ag/GO/TNR substrate is illustrated in Scheme 3. In the degradation of R6G, the synergistic effect of three components leads to excellent photocatalytic performance. The partially oxidized GO interlayer between Ag and TNR is reserved as an electron reservoir and a transfer path. In this system, the R6G molecules are primarily degraded in two steps: the absorption of light by the substrate and the photo-generation of free radicals that produce molecular oxidization. Generally speaking, the simulated sunlight primarily consists of UV light and visible light. For the Ag/GO/TNR substrate, the photogenerated carriers are generated via two photocatalytic routes under simulated sunlight. One route involves the excited TNR that generates electron and hole pairs with the irradiation from UV light. Due to the close contact of the TNR and GO nanosheets, the electrons can transfer from the TNR to the GO. Additionally, the electrons may further transfer from the GO to the Ag NPs because the work function of the Ag NPs (about 4.2 eV) is lower than that of GO (about 4.7 eV) [68–70]. The transfer process will help to quicken electron-hole separation and suppress carrier recombination. After a series of chain reactions, these free radicals will bring powerful active radicals, such as $^{\cdot}O_2^-$, $h^+$ and $^{\cdot}OH$, to degrade the MO molecules. In this case, the GO nanosheets offer a rapid electron transfer path, and the Ag NPs act as an electron reservoir, accelerating charge separation. On the other hand, Ag NPs with surface plasmon resonance can excite the electrons by visible light. The work

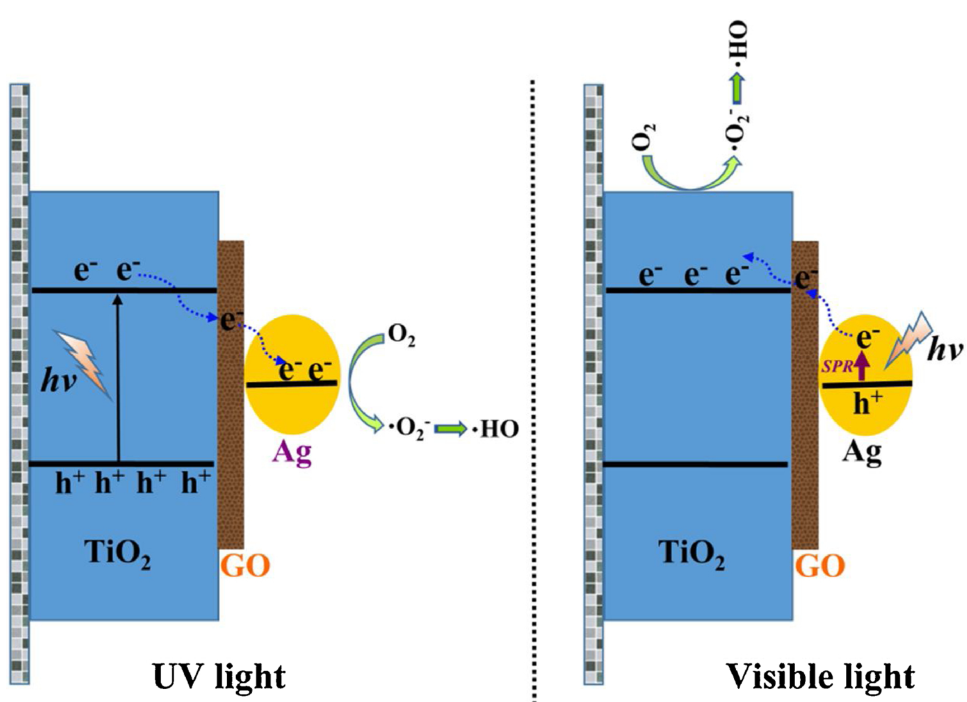


**Scheme 3.** A possible photodegradation mechanism of R6 G molecules on Ag/GO/TNR substrate.

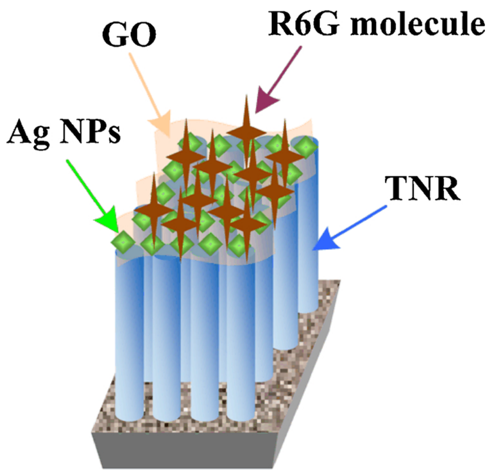


**Scheme 4.** A sketch of Ag/GO/TNR as SERS substrate for R6 G detection.

functions of TNR and GO are different from that of Ag, so the photo-excited electrons are from the Ag NPs to GO and from GO to CB of the TNR. In this case, the GO nanosheets serve as electron reservoirs for the Ag/GO/TNR. Moreover, during the photocatalytic process, the loss of oxygen functional groups can lead to the decreased bandgap and the increased conductivity for GO. It may further inhibit the recombination of photo-generated electrons and holes [71–74]. Through the above photocatalytic mechanisms, the effective electron transfer at the interfaces of the Ag NPs, GO, and TNR films results in an excellent photocatalytic performance under simulated sunlight.

It is well known that the SERS enhancement mechanism primarily includes the EM and CM effect. Scheme 4 shows a schematic of the Ag/GO/TNR as a SERS substrate for R6 G detection. In this system, the enhanced Raman signals of the Ag/GO/TNR active substrate are due to the synergistic effect of three components. First, due to the large specific surface area, GO interlayers attached to the surface of the TNR can provide a large adhesion area for Ag NPs. Therefore, more R6 G molecules can be absorbed on the substrate for improving SERS performance. Second, GO nanosheets and Ag NPs are successively deposited on the surface of the TNR with a rich structure. This process results in a significant roughness of the substrate. Such a particular multiple structure can act like light traps, making it easy for incident photons produced by the excited light to bounce off several times during SERS detection. Thus, a single photon may have multiple contacts with the surface of Ag NPs, which can generate a significant SERS effect in the active substrate. Third, in addition to the large adhesion area and interaction of excited photons, the local surface electromagnetic field provided by the Ag NPs is the main source of SERS activity for the Ag/GO/TNR substrate. There are two main areas of surface local electromagnetic fields in Ag NPs. One is Ag NPs sites with large surface curvature, and the other is small areas with less than 50 nm of spacing between adjacent Ag NPs. As can be seen from the above SEM and TEM images, Ag NPs grown on the surface of the GO/TNR have many tips with large curvature, and many small regions less than 50 nm exist in the substrate. Such a structure possesses a lot of high-density hotspots in the entire surface of the substrate, which significantly improves SERS activity. Moreover, the existence of some Ag dimers on the substrate can generate local SPR due to the coupling of surface plasmas, contributing to the enhancement of Raman signals. Furthermore, the charge transfer between GO and R6 G can contribute to higher SERS enhancement.

## 4. Conclusions

In conclusion, a novel graphene oxide/$TiO_2$ nanorod array decorated with Ag nanoparticles was successfully designed as a dual-functional substrate for SERS detection and photocatalysis of organic molecules. It was found that GO interlayer played a key effect on the microstructure and properties of the Ag/GO/TNR substrate. The Ag/GO/TNR with 5 min of GO-deposition exhibited an adsorption ratio of 44% R6 G, showing a higher adsorption capacity and larger surface area. The detection limit of R6 G was as low as $1.0 \times 10^{-12}$ M, and the value of EF was as up to $5.86 \times 10^5$, exhibiting the improved SERS sensitivity of the Ag/GO/TNR. Furthermore, the Ag/GO/TNR substrate also exhibited good uniformity with an RSD value of 8.71%. In addition, the photocatalytic activity of the substrate effectively decomposed R6 G molecules adsorbed on the surface after Xenon lamp irradiation, indicating a self-cleaning property of the Ag/GO/TNR substrate. After three cycling measurements, the Raman signals for the Ag/GO/TNR were almost unchanged. In the photodegradation of R6 G, the Ag/GO/TNR film showed a maximum k of 0.012015 $min^{-1}$, which is 3.59 and 2.3 times higher than those of TNR and Ag/TNR. The present work not only demonstrated a facile method to obtain Ag/GO/TNR film, but also provided an easy and effective route for the preparation of SERS-active substrates with high sensitivity, good uniformity, photocatalytic activity and reusability, which is expected to have potential application in the detection of molecules.

## Acknowledgments

This work was financially supported by the National Natural Science Foundation of China (No. 51772003, 51472003, 51701001, 51702003), Provincial Natural Science Foundation of Anhui Higher Education Institution of China (No. KJ2017A002,1808085ME130).

## Appendix A. Supplementary data

Supplementary material related to this article can be found, in the online version, at doi:https://doi.org/10.1016/j.apcatb.2019.03.084.

## References

[1] R.A. Halvorson, P.J. Vikesland, Environ. Sci. Technol. 44 (2010) 7749–7755.
[2] Z. Li, S. Jiang, S. Xu, C. Zhang, H. Qiu, C. Li, B. Man, Sens. Actuators B Chem. 230 (2016) 645–652.
[3] B.R. Yu, M.H. Ge, P. Li, Q.W. Xie, L.B. Yang, Talanta 191 (2019) 1–10.
[4] K. Mao, Z.L. Zhou, S. Han, X.D. Zhou, J.M. Hu, X.Q. Li, Z.G. Yang, Talanta 190 (2018) 263–268.
[5] M.K. Fan, G.F.S. Andrade, A.G. Brolo, Anal. Chim. Acta 693 (2011) 7–25.
[6] S. Shanmukh, L. Jones, J. Driskell, Y.P. Zhao, R. Dluhy, R.A. Tripp, Nano Lett. 6 (2006) 2630–2636.
[7] L. Zhang, J.S. Hu, X.H. Huang, J. Song, S.Y. Lu, Nano Energy 48 (2018) 489–499.
[8] Y. Xu, F.Y.H. Kutsanedzie, M.M. Hassan, H.H. Li, Q.S. Chen, Spectrochim. Acta A. 206 (2019) 405–412.
[9] D.A. Jency, R. Parimaladevi, A.A.J. Amali, G.V. Sathe, M. Umadevi, Colloid. Surface. A 554 (2018) 218–226.
[10] L. Zhang, J.S. Hu, X.H. Huang, J. Song, S.Y. Lu, J. Alloy Compd. 735 (2018) 660–667.
[11] K.C. Hsu, D.H. Chen, ACS Appl. Mater. Interfaces 7 (2015) 27571–27579.
[12] Y.C. Ko, H.Y. Fang, D.H. Chen, J. Alloy Compd. 695 (2017) 1145–1153.
[13] L. Chen, B. Duan, J. Liu, Z. Gu, Q. Luo, C.Y. Duan, RSC Adv. 6 (2016) 38690–38696.
[14] W.H. Li, R. Zamani, P.R. Gil, B. Pelaz, M. Ibáñez, D. Cadavid, A. Shavel, R.A. Alvarez-Puebla, W.J. Parak, J. Arbiol, A. Cabot, J. Am. Chem. Soc. 135 (2013) 7098–7101.
[15] S.P. Wen, Y. Su, R. Wu, S.W. Zhou, Q.H. Min, G.C. Fan, L.P. Jiang, R.B. Song, J.J. Zhu, Biosen. Bioelectron 117 (2018) 260–266.
[16] X. Jiang, Y. Chen, J. Du, X. Li, Y. Shen, M. Yang, X.X. Han, L.B. Yang, B. Zhao, J. Raman Spectrosc. 49 (2018) 1257–1264.
[17] M.M. Zalduendo, J. Langer, J.J. Giner-Casares, E.B. Halac, G.J.A.A. Soler-Illia, L.M. Liz-Marzán, P.C. Angelomé, J. Phys. Chem. C 122 (2018) 13095–13105.
[18] Y.Y. Sun, L.L. Yang, F. Liao, Q. Dang, M.W. Shao, Appl. Surf. Sci. 443 (2018) 613–618.
[19] L.L. Yang, Q.Q. Sang, J. Du, M. Yang, X.L. Li, Y. Shen, X.X. Han, X. Jiang, B. Zhao, Phys. Chem. Chem. Phys. 20 (2018) 15149–15157.
[20] T.L. Guo, J.G. Li, X.D. Sun, Y. Sakka, Appl. Surf. Sci. 423 (2017) 1–12.
[21] H. Rajput, V.K. Sangal, A. Dhir, J. Electroanal. Chem. 814 (2018) 118–126.
[22] X.W. Li, H.F. Xu, L. Wang, L. Zhang, X.F. Cao, Y.C. Guo, J. Taiwan Inst. Chem. E. 85 (2018) 257–264.
[23] Y. Jiang, J. Wang, L. Malfatti, D. Carboni, N. Senes, P. Innocenzi, Appl. Surf. Sci. 450 (2018) 451–460.
[24] Z. Li, S.Z. Jiang, Y.Y. Huo, T.Y. Ning, A.H. Liu, C. Zhang, Y. He, M.H. Wang, C.H. Li,

Baoyuan Man, Nanoscale 10 (2018) 5897–5905.
[25] X.L. Zhang, N. Wang, R.J. Liu, X.Y. Wang, Y. Zhu, J. Zhang, Opt. Mater. Express 8 (2018) 704–717.
[26] G.C. Shi, M.L. Wang, Y.Y. Zhu, L. Shen, Y.H. Wang, W.L. Ma, Y. Chen, R.F. Li, Opt. Commun. 412 (2018) 28–36.
[27] X. Fu, F. Bei, X. Wang, L. Lu, J. Raman Spectrosc. 41 (2010) 370–373.
[28] X.Z. Wang, Z. Wang, X.S. Jiang, J.J. Tao, Z.Z. Gong, Y.L. Cheng, M. Zhang, L. Yang, J.G. Lv, G. He, Z.Q. Sun, J. Electrochem. Soc. 163 (2016) 943–950.
[29] Y.F. Wang, M. Zhang, L.L. Fang, H.C. Yang, Y. Zong, J. Gao, G. He, Z.Q. Sun, J. Am. Ceram. Soc. 00 (2018) 1–14.
[30] Z. Li, S.Z. Jiang, Y.Y. Huo, T.Y. Ning, A.H. Liu, C. Zhang, Y. He, M.H. Wang, C.H. Li, B.Y. Man, Nanoscale 10 (2018) 5897–5905.
[31] Z.F. Zhao, Y.Z. Wang, J. Xu, Y. Wang, RSC Adv. 5 (2015) 59297–59305.
[32] L. Shang, T. Bian, B.H. Zhang, D.H. Zhang, L.Z. Wu, C.H. Tung, Y.D. Yin, T.R. Zhang, Angew. Chem. Int. Edit. 53 (2014) 250–254.
[33] Y. Song, K. Qu, C. Zhao, J. Ren, X. Qu, Adv. Mater. 22 (2010) 2206–2210.
[34] M.G. Wang, J. Han, H.X. Xiong, R. Guo, Y.D. Yin, ACS Appl. Mater. Interfaces 7 (2015) 6909–6918.
[35] G.I.N. Waterhouse, G.A. Bowmaker, J.B. Metson, Appl. Surf. Sci. 183 (2001) 191–204.
[36] M. Sametband, I. Kalt, A. Gedanken, R. Sarid, ACS Appl. Mater. Interfaces 6 (2014) 1228–1235.
[37] P. Anil Kumar Reddy, C. Manvitha, R. Boddula, S.V. Prabhakar Vattikuti, M. Kotesh Kumar, C. Byon, Mater Res. Bull. 98 (2018) 314–321.
[38] J.H. He, I. Ichinose, S. Fujikawa, T. Kunitake, A. Nakao, Chem. Commun. 19 (2002) 1910–1911.
[39] X. Zhao, W.W. Zhang, C.C. Peng, Y.J. Liang, W.Z. Wang, J Colloid Interf. Sci. 507 (2017) 370–377.
[40] T.F. Yeh, J.M. Syu, C. Cheng, T.H. Chang, H. Teng, Adv. Funct. Mater. 20 (2010) 2255–2262.
[41] T.F. Yeh, F.F. Chan, C.T. Hsieh, H. Teng, J. Phys. Chem. C 115 (2011) 22587–22597.
[42] Y. Chen, X.Q. Xie, X. Xin, Z.R. Tang, Y.J. Xu, ACS Nano 13 (2019) 295–304.
[43] S.H. Li, N. Zhang, X.Q. Xie, R. Luque, Y.J. Xu, Angew. Chem. Int. Ed. 57 (2018) 13082–13085.
[44] N. Zhang, M.Q. Yang, S.Q. Liu, Y.G. Sun, Y.J. Xu, Chem. Rev. 115 (2015) 10307–10377.
[45] C. Han, N. Zhang, Y.J. Xu, Nano Today 11 (2016) 351–372.
[46] J. Ito, J. Nakamura, A. Natori, J. Appl. Phys. 103 (2008) 113712.
[47] S.F. Chen, J.P. Li, K. Qian, W.P. Xu, Y. Lu, W.X. Huang, S.H. Yu, Nano Res. 3 (2010) 244–255.
[48] M. G. Wang, J. Han, H.X. Xiong, R. Guo, Langmuir 31 (2015) 6220–6228.
[49] J.J. Tao, Z.Z. Gong, G. Yao, Y.L. Cheng, M. Zhang, J.L. Lv, S.W. Shi, G. He, X.S. Chen, Z.Q. Sun, J. Alloy Compd. 689 (2017) 451–459.
[50] Y.C. Wu, Z.M. Liu, Y.R. Li, J.T. Chen, X.X. Zhu, P. Na, Mater. Lett. 240 (2019) 47–50.
[51] H.Y. Tian, G.H. Zhao, Y.N. Zhang, Y.B. Wang, T.C. Cao, Electrochim. Acta 96 (2013) 199–205.
[52] X.Z. Wang, Z. Wang, M. Zhang, X.S. Jiang, Y.F. Wang, J.G. Lv, G. He, Z.Q. Sun, J. Alloy Compd. 725 (2017) 1166–1174.
[53] H. Fang, C.X. Zhang, L. Liu, Y.M. Zhao, H.J. Xu, Biosens. Bioelectron. 64 (2015) 434–441.
[54] L.M. Chen, L.B. Luo, Z.H. Chen, M.L. Zhang, J.A. Zapien, C.S. Lee, S.T. Lee, Phys. Chem. C 114 (2010) 93–100.
[55] K.S. Hui, K.N. Hui, D.A. Dinh, C.H. Tsang, Y.R. Cho, W. Zhou, H.H. Chun, Acta Mater. 64 (2014) 326–332.
[56] K.C. Hsu, D.H. Chen, ACS Appl. Mater. Interfaces 7 (2015) 27571–27579.
[57] Q. Yang, M.M. Deng, H.Z. Li, M.Z. Li, C. Zhang, W.Z. Shen, Y.N. Li, D. Guo, Y.L. Song, Nanoscale 7 (2014) 421–425.
[58] H. Kang, A. Kulkarni, S. Stankovich, R.S. Ruoff, S. Baik, Carbon 47 (2009) 1520–1525.
[59] R.J.W.E. Lahaye, H.K. Jeong, C.Y. Park, Y.H. Lee, Phys. Rev. B 79 (2009) 125435.
[60] S. Stankovich, D.A. Dikin, R.D. Piner, K.A. Kohlhaas, A. Kleinhammes, Y. Jia, Y. Wu, S.T. Nguyen, R.S. Ruoff, Carbon 45 (2007) 1558–1565.
[61] S. Gilje, S. Han, M. Wang, K.L. Wang, R.B. Kaner, Nano Lett. 7 (2007) 3394–3398.
[62] C. Gmez-Navarro, R.T. Weitz, A.M. Bittner, M. Scolari, A. Mews, M. Burghard, K. Kern, Nano Lett. 7 (2007) 3499–3503.
[63] H.K. Jeong, Y.P. Lee, R.J.W.E. Lahaye, M.H. Park, K.H. An, I.J. Kim, C.W. Yang, C.Y. Park, R.S. Ruoff, Y.H.J. Lee, Am. Chem. Soc. 130 (2008) 1362–1366.
[64] I. Jung, D.A. Dikin, R.D. Piner, R.S. Ruoff, Nano Lett. 8 (2008) 4283–4287.
[65] D.W. Boukhvalov, M.I.J. Katsnelson, Am. Chem. Soc. 130 (2008) 10697–10701.
[66] G. Lu, L.E. Ocola, J. Chen, Nanotechnology 20 (2009) 445502.
[67] G. Eda, G. Fanchini, M. Chhowalla, Nat. Nanotechnol. 3 (2008) 270–274.
[68] Y.T. Li, L.L. Qu, D.W. Li, Q.X. Song, F. Fathi, Y.T. Long, Biosens. Bioelectron. 43 (2013) 94–100.
[69] X. Zhang, N. Wang, R.J. Liu, X.Y. Wang, Y. Zhu, J. Zhang, Opt. Mater. Express 8 (2018) 704–717.
[70] M.G. Wang, J. Han, H.X. Xiong, R. Guo, Langmuir 31 (2015) 6220–6228.
[71] N. Zhang, M.Q. Yang, Z.R. Tang, Y.J. Xu, ACS Nano 8 (2013) 623–633.
[72] K.Q. Lu, L. Yuan, X. Xin, Y.J. Xu, Appl. Catal. B-Environ. 226 (2018) 16–22.
[73] N. Lv, Y.Y. Li, Z.L. Huang, T. Li, S.Y. Ye, D.D. Dionysiou, X.L. Song, Appl. Catal. B-Environ. 246 (2019) 303–311.
[74] R. Boppella, S.T. Kochuveedu, H. Kim, M.J. Jeong, F.M. Mota, J.H. Park, D.H. Kim, ACS Appl. Mater. Interfaces 9 (2017) 7075–7083.